Enhanced Light Absorption by Facile Patterning of Nano-grating on Mesoporous TiO2 Photoelectrode for Cesium Lead Halide Perovskite Solar Cells

Sungho Woo (shwoo@dgist.ac.kr)
Daegu Gyeongbuk Institute of Science and Technology
Kang-Pil Kim
DGIST: Daegu Gyeongbuk Institute of Science and Technology
Soo Min Kwon
DGIST: Daegu Gyeongbuk Institute of Science and Technology
Wook Hyun Kim
DGIST: Daegu Gyeongbuk Institute of Science and Technology

Nano Express

Keywords: CsPbIBr2, perovskite solar cell, mesoporous TiO2, nanoimprinting, grating nanopattern, increased light absorption

Posted Date: October 2nd, 2020

DOI: https://doi.org/10.21203/rs.3.rs-84465/v1

Abstract

$CsPbIBr_2$, a type of cesium based all-inorganic halide perovskite (CsPe) composition, has been proposed as an alternative perovskite material against the mainstream organic–inorganic hybrid halide perovskite (HPe) materials owing to its exceptional humidity, thermal, temperature, and light stability. However, the low power conversion efficiency (*PCE*) due to its wide bandgap (2.05 eV) is an obstacle for its application in developing highly efficient solar cells. In this study, facile nanoimprinted one-dimensional grating nanopattern (1D GNP) formation on mesoporous TiO_2 (mp-TiO_2) photoelectrode has been introduced to improve the effective light utilization for enhancing the performance of $CsPbIBr_2$ perovskite solar cells (PSCs). The 1D GNP structure on mp-TiO_2 layer can not only increase the light absorption efficiency by diffracting the unabsorbed light into the mp-TiO_2 and $CsPbIBr_2$ active layer, but can also increase the charge separation and collection due to the enlarged interfacial contact area between the mp-TiO_2 and $CsPbIBr_2$ layers. Consequently, both current density (J_{SC}) and fill factor (*FF*) of the fabricated cells were improved leading to over 20% improvement in their *PCE*. Thus, we conclude that this periodic grating structure, fabricated by simple solvent-assisted nanoimprinting, can play an important role in the realization of high-efficiency and low-cost Cs-based PSCs.

1. Introduction

The organic–inorganic hybrid halide perovskite (HPe) solar cells have achieved impressive power conversion efficiency (*PCE*) of over 25% during the last ten years [1,2]. This remarkable progress is mainly attributed to their outstanding properties, which are intense broadband light absorption, high charge carrier mobility, and long charge diffusion length [1,3]. HPe has a typical structure of ABX_3, where A is an organic cation (mainly $CH_3NH_3^+$ (MA^+) and/or $NH_2CHNH_2^+$ (FA^+)), B is an inorganic cation (Pb^{2+}, Ge^{2+}, Sn^{2+}), and X is a halogen anion (I^-, Br^-, Cl^-). Although HPe has achieved very high *PCE*, its thermal, light, and moisture stability is not sufficient for device commercialization owing to the intrinsically volatile and hygroscopic nature of the organic cation moieties, such as MA^+ or FA^+ [4].

To solve this problem, several methods have been developed, including metal doping into perovskite phase [7], interface/surface treatment [6], device encapsulation technique [5], and employing an all-inorganic perovskite composition [8-10]. Among these methods, the generally accepted effective way is to replace the volatile organic group by inorganic cesium (Cs) cations to make a Cs-based all-inorganic perovskite (CsPe) light-absorption layer. For example, CsPe ($CsPbX_3$, X = I, Br, Cl, or their mixture) based perovskite solar cells (PSCs) have shown remarkable stability under 80% humidity or 100 °C heating conditions [11,12]. The efficiency of $CsPbX_3$ is closely related to its halide composition, which leads to a change in its crystal structure, band gap, and humidity tolerance. The currently studied inorganic perovskite compositions are mainly $CsPbI_3$, $CsPbI_2Br$, $CsPbIBr_2$, and $CsPbBr_3$, based on the type of halide and its ratio. Among these all-inorganic Cs-based perovskites, the α-phase $CsPbI_3$ is the most widely investigated perovskite owing to its favorable narrow band gap (E_g = 1.73 eV) and excellent efficiency of

17.06%. However, the black α-phase $CsPbI_3$ suffers from severe instability and easily degrades to a non-perovskite yellow δ-phase $CsPbI_3$ (E_g = 2.82 eV), even at room temperature. These are the major issues that delimit the fabrication of solar cell devices using $CsPbI_3$ [13,14]. On the other hand, the $CsPbBr_3$ PSCs have shown excellent stability, even without any encapsulation. However, a $CsPbBr_3$ layer shows a terrible light absorption only up to 540 nm due to its wide band gap (E_g = 2.3 eV), which leads to a lower *PCE* [15]. Therefore, exchanging some iodide ions with bromide ions in CsPe to form a mixed halide CsPe ($CsPbI_{3-x}Br_x$) could be a good alternative for improving the phase stability. $CsPbI_2Br$, one of the mixed halides CsPe, has a narrow band gap of 1.92 eV and shows better stability than that of $CsPbI_3$; however, for $CsPbI_2Br$, overcoming the stability issue is still a challenge [16,17]. Finally, $CsPbIBr_2$ (another mixed halide CsPe) has been considered as the best choice among all the possible Cs-based inorganic perovskites because it can balance the acceptable band gap of 2.05 eV and possess a superior phase stability in air. Moreover, $CsPbIBr_2$ has a typical bright red color that is suitable for applications in tandem devices and colorful smart photovoltaic windows [18,19]. Over the years, the *PCE* of $CsPbIBr_2$ has developed from the initial state of 4.7% to the recent highest state of 10.88% by introducing various strategies, such as modification of the fabrication process to obtain a better film quality, interface/surface engineering and elemental impurity doping for energy-level control and good charge carrier transport [19-23]. Although the cell performance of $CsPbIBr_2$ is significantly improved through these effective modifications, its *PCE* is still restricted as compared to that of the organic–inorganic hybrid PSCs. This limited *PCE* is caused by a poor light absorption wavelength edge of 600 nm due to its intrinsic wide band gap. To address this limited light-absorption characteristic, several photon management techniques, such as the surface plasmonic effect, anti-reflection concept, and periodic grating have been applied and studied to increase the time of residence of the targeted photons into the photoactive layer [24-27]. Considering the results of these previous studies, we can conclude that a promising approach to improve the light absorption of a wide band gap $CsPbIBr_2$ (without increasing its thickness) is to trap the incident light and increase the light-dwelling time in the active layer by employing a periodic grating.

In this study, we have introduced one-dimensional grating nanopattern (1D GNP) on the top of a mesoporous TiO_2 (mp-TiO_2) layer by solvent-assisted nanoimprinting and incorporated it into $CsPbIBr_2$ PSCs to improve their light harvest as well as charge collection. As a result, the device with a flat mp-TiO_2 layer exhibited a *PCE* of 3.5% while the device with 1D GNP mp-TiO_2 layer showed a *PCE* of 4.3%, which is a ~23% improvement in the *PCE* due to an increase in the photogenerated current density (J_{SC}) and fill factor (*FF*) of the $CsPbIBr_2$ PSCs.

2. Methods/experimental

Materials used and nanopatterned PDMS mold preparation

CsI (99.9%), $PbBr_2$ (99.999%), chlorobenzene (anhydrous, 99.8%), Dimethyl sulfoxide (DMSO, anhydrous, greater than 99.9%), and Trichloro(1H,1H,2H,2H-perfluorooctyl)silane (PFOCTS, 97%) were purchased from Sigma-Aldrich. TiO_2 solution of SC-BT060 and SC-HT040 (particle size 50 nm) were purchased from Sharechem Co. (South Korea) to fabricate a blocking-TiO_2 (bl-TiO_2) layer and mp-TiO_2 layer, respectively. Poly[[4,8-bis[(2-ethylhexyl)oxy]benzo[1,2-b:4,5-b']dithiophene-2,6-diyl][3-fluoro-2-[(2-ethylhexyl)carbonyl]thieno[3,4-b]thiophenediyl]] (PTB7, weight-average molecular weight = 116 kDa, polydispersity index = 2.5) was purchased from 1-Material Inc. All chemicals were used in the form as delivered by the manufacturer without further purification.

To prepare a 1D GNP prepatterned polydimethylsiloxane (PDMS) mold, the silicon (Si) master (29 mm x 24.2 mm, period 605 nm, groove depth 190 nm, LightSmyth Technologies Inc.) was put in a Petri dish. A few drops of PFOCTS was used to make the Si master surface hydrophobic to facilitate easy removal of the Si master from the PDMS mold. Next, the PDMS pre-polymer was prepared by mixing elastomer base (Sylgard 184, Dow Corning) and curing agent in a ratio of 10:1 (wt/wt) and followed by degassing for 1 h. Then, the PDMS pre-polymer was poured onto the Si master followed by curing at 100 ^oC for 40 min. Finally, the cured PDMS mold was separated from the Si master and used for nanopatterning of the mp-TiO_2 layer.

Device fabrication

Fig. 1 Schematics of (a) the device structure of $CsPbIBr_2$ perovskite solar cells with a flat mp-TiO_2 and 1D GNP mp-TiO_2, and (b) the fabrication process for 1D GNP mp-TiO_2.

The $CsPbIBr_2$ solar cells, fabricated and examined in this study, have a typical structure of FTO/bl-TiO_2/mp-TiO_2/$CsPbIBr_2$/PTB7/Au, where PTB7 is employed as a hole transport layer (HTL) (see Fig. 1(a)). The bl-TiO_2 layer (30 nm) was deposited onto a cleaned FTO surface by spin-coating a TiO_2 solution (SC-BT060) at 3000 rpm for 30 s, followed by annealing at 500 °C for 30 min in air. The mp-TiO_2 layer (300 nm) was deposited on the bl-TiO_2/FTO glass substrates by spin-coating a TiO_2 paste (SC-HT040) at 3000 rpm for 30 s annealed at 500 °C for 30 min.

For 1D GNP mp-TiO_2, the PDMS mold was quickly placed onto a spin-coated mp-TiO_2 paste with proper pressure to employ solvent-assisted nanoimprinting from the partially wet surface. Next, the substrate was dried at 125 °C for 5 min to remove the residual solvent, followed by detaching the PDMS mold and then, the nanopatterned mp-TiO_2 film was annealed at 500 °C for 30 min (see Fig. 1(b)).

To prepare the $CsPbIBr_2$ layer, a precursor solution (1 M solution of CsI and $PbBr_2$ in DMSO) was spin-coated on the mp-TiO_2 layer at 2500 rpm for 60 s and annealed at 160 ^oC for 20 min. Subsequently, PTB7 solution (5 mg in 1 mL chlorobenzene) was spin-coated on the $CsPbIBr_2$ layer at a speed of 3000 rpm for 60 s, which was then heated on a hot plate at 70 °C for 30 min in air. Finally, the Au counter electrode (70

nm) was deposited using a thermal evaporator under a pressure of 5.0×10^{-6} Torr. Each fabricated device had an active area of 0.16 cm^2.

Measurement and analysis

The cross-sectional and top view images of the mp-TiO_2 layer were characterized using field emission scanning electron microscopy (FE-SEM, S-4800, Hitachi). The optical properties of mp-TiO_2 were determined using a UV-Vis spectrometer (Lambda 750, Perkin Elmer). The structural information of $CsPbIBr_2$ perovskite layer was characterized by a multi-purpose X-ray diffraction (XRD) system (Empyrean, PANalytical) with θ-2θ mode at a scan rate of 0.05^o/sec. The current density–voltage ($J–V$) characteristics were measured using a specialized solar cell measurement system equipped with an electrometer (model 2400, Keithley) and solar simulator (91192, Newport) with a 1 kW xenon arc lamp (Oriel). The light intensity was adjusted to one sun (100 mW/cm^2) under AM 1.5G solar irradiation condition using a radiant power energy meter (model 70260, Oriel). The series resistance (R_S) and shunt resistance (R_{SH}) were calculated from the slope of the corresponding $J–V$ curves beyond V_{OC} and J_{SC}, respectively. The external quantum efficiency (EQE) was measured by a QuantX-300 quantum efficiency measurement system (Newport) equipped with a 100 W xenon lamp.

3. Results And Discussion

The mp-TiO_2 with 1D GNP structure shows rainbow-colored visual effect due to optical interference by the grating nanopattern (see the bottom inset of Fig. 1(b)).

Fig. 2(a) and 2(b) show the SEM image of the mp-TiO_2 layer, with and without the 1D GNP structure. The cross-sectional and top view images of the 1D GNP mp-TiO_2 show a clear periodic pattern over the entire large-area without fragments or cracks during detaching the PDMS mold from the mp-TiO_2 surface. The period, width, and height of the 1D GNP mp-TiO_2 are about 610 nm, 250 nm, and 120 nm, respectively. XRD measurements were performed to reveal the formation of the $CsPbIBr_2$ perovskite layer (Fig. 2(c)). The typical diffraction peaks in the XRD patterns were matched to α-phase $CsPbIBr_2$, and were found to be consistent with those of the previous reports. Three dominant diffraction peaks at 15.02°, 21.27°, and 30.15° that are indexed to the (100), (110), and (200) planes, respectively show the good crystallinity and morphology formation in the $CsPbIBr_2$ perovskite layer, which are further confirmed from the SEM image in the inset of Fig. 2(c) [20,28-30].

Fig. 2 (a) Cross-section and top view SEM images of the flat mp-TiO_2 and (b) 1D GNP mp-TiO_2. (c) XRD data for the $CsPbIBr_2$ layer (inset shows the surface morphology of the $CsPbIBr_2$ layer).

Fig. 3(a) and Table 1 show the $J–V$ characteristics for the devices with and without 1D GNP pattern under AM 1.5G illumination (100 mW/cm^2). The efficiency of the $CsPbIBr_2$ solar cell was improved by introducing 1D GNP into the mp-TiO_2 layer.

The flat mp-TiO_2 device had a *PCE* of 3.5%, V_{OC} of 0.971 V, J_{SC} of 7.98 mA/cm^2, and *FF* of 45.17%. However, in the 1D GNP mp-TiO_2 device, all these parameters increased, i.e., V_{OC}, J_{SC}, and *FF* increased to 0.975 V, 8.88 mA/cm^2, and 49.73%, respectively, leading to a *PCE* of 4.31%. The introduction of 1D GNP pattern resulted in ~23% improvement in the *PCE* primarily due to the improvement in J_{SC}. (Here, we note that although there is a large difference in *PCE* from the recently reported best efficiency of 10.88% [18,22], our device efficiency of ca. 4% is reasonable because we made them via the very basic one-step coating process without using any improved methods, such as anti-solvent dropping, interface treatment, impurity doping, etc.)

Fig. 3 Current density–voltage (J–V) characteristics of $CsPbIBr_2$ solar cells with a flat mp-TiO_2 and a 1D GNP mp-TiO_2 under (a) one sun illumination and (b) dark condition.

Table 1 Summary of device performance with a flat mp-TiO_2 and 1D GNP mp-TiO_2 under AM 1.5G condition.

Device	J_{SC}(mA/cm^2)	V_{OC}(V)	*FF* (%)	*PCE* (%)	R_S(Ωcm^2)	R_{SH}(Ωcm^2)
Flat mp-TiO_2	7.98	0.971	45.17	3.50	37.21	1272.73
1D GNP mp-TiO_2	8.88	0.975	49.73	4.31	25.98	1773.91

Fig. 4 (a) Reflectance, (b) transmittance, and (c) absorbance spectra of the flat mp-TiO_2 and 1D GNP mp-TiO_2 layers.

To study the mechanism behind these improvements, further investigations of optical and electrical properties of the devices were conducted. First, we measured the reflectance, transmittance, and absorbance of the glass/FTO/bl-TiO_2/mp-TiO_2 samples to study the effect of 1D GNP on optical properties of mp-TiO_2 using a UV–Vis spectrometer in the wavelength range from 300 to 700 nm, where the beam was incident on the glass side. The measured reflectance of mp-TiO_2 with 1D GNP was higher than that of the flat mp-TiO_2, as shown in Fig. 4(a). On the contrary, the transmittance of mp-TiO_2 with 1D GNP is lower than that of the flat mp-TiO_2. Therefore, the 1D GNP mp-TiO_2 can absorb more light than the flat one over a broad range of wavelengths (see Fig. 4(b) and 4(c)) [31,32]. This is attributed to the increased optical path-length and light trapping effect by diffracting the unabsorbed light back into the mp-TiO_2 photoelectrode at an oblique angle, which can further result in enhanced photon absorption in the $CsPbIBr_2$ active layer.

Compared to flat mp-TiO_2, we can see the obvious light diffraction effect of 1D GNP mp-TiO_2 from the corresponding digital camera images in Fig. 5.

When light is incident on the grating interface, it scatters into multiple transmitted and reflected orders (m = …, −2, −1, 0, 1, 2, …), as illustrated in Fig. 5(c). Each order represents a different direction for the

scattered light, and the zeroth order (m = 0) represents the light scattered in the same direction as the incident light [33]. Fig. 5(a) and 5(b) show the diffracted and reflected light by flat mp-TiO_2 and 1D GNP mp-TiO_2 using He-Ne laser (632.8 nm). In Fig. 5(a) and 5(b), we can observe the reflected light on glass surface and diffracted light on the front black screen in the case of 1D GNP mp-TiO_2, whereas flat mp-TiO_2 shows only a strong transmitted light without the diffracted and reflected light. Additionally, the zeroth order transmitted light of the 1D GNP mp-TiO_2 is weaker than that of the flat mp-TiO_2, which corresponds to the reflectance and transmittance spectra in Fig. 4(a) and (b). Furthermore, if the angle of reflected–diffracted light is larger than the critical angle for total internal reflection because of slightly decreased refractive index values from mp-TiO_2 to air (i.e. $n_{mp\text{-}TiO2}$ (≈ 2.1) > n_{FTO} (≈ 1.9) > n_{Glass} (≈ 1.5) > n_{Air} (= 1.0), where these refractive index values at 550 nm were estimated from the previous reports [34,35]), then the light can be reflected back to the mp-TiO_2 and perovskite layer leading to an additional absorption, as illustrated in Fig. 5(c).

Fig. 5 Digital camera images of diffracted light from (a) flat mp-TiO_2 and (b) 1D GNP mp-TiO_2, and (c) schematic illustration of grating diffraction.

Next, we performed the EQE measurement to confirm that current enhancement is the main factor for increasing the device performance in 1D GNP mp-TiO_2 structure. As shown in Fig. 6(a), an enhancement over the entire spectral range was observed for the devices with 1D GNP structure. These results indicate that 1D GNP structures induce more photogenerated charge carriers by enhanced absorption of incident light, resulting from an increase in optical path-length and light trapping.

Fig. 6 (a) External quantum efficiency (EQE) spectra and (b) *PCE* distribution histogram of the $CsPbIBr_2$ PSCs with and without 1D GNP structure in mp-TiO_2 for 20 devices.

Contrarily, the device with 1D GNP mp-TiO_2 showed higher *FF* in comparison with the controlled flat mp-TiO_2 device. Therefore, we calculated internal resistances of the devices (i.e. R_S and R_{SH}) from the light *J-V* curve, and also measured the dark *J-V* characteristic to study the effect of 1D GNP on the device resistance. The higher *FF* of the 1D GNP may have been caused by the reduced interface resistance due to the increase in the contact area between the 1D GNP mp-TiO_2 and $CsPbIBr_2$ active layer, as demonstrated in the dark *J-V* curves in Fig 3(b). The decreased R_S and increased R_{SH} indicate better charge transport that can be another factor causing the observed high *FF* in the devices with 1D GNP mp-TiO_2 [34,36].

Finally, we fabricated and tested 20 perovskite solar cells, with and without the 1D GNP mp-TiO_2 layer, to compare the performance enhancement exhibited by the 1D nanostructures. The photovoltaic characteristics of the fabricated devices are plotted in histograms, as shown in Fig. 6(b). We can see the consistent and reproducible *PCE* improvement trend in the case of 1D GNP mp-TiO2 structure.

Conclusions

We have successfully introduced a 1D GNP structure on mp-TiO_2 for fabricating high performance $CsPbIBr_2$ perovskite solar cells using a simple nanoimprinting method with a PDMS mold. It is evident from the UV-Vis spectra and EQE measurement data that the 1D GNP structure can diffract the incident light to increase optical path-length within the mp-TiO_2 and active layers leading to an enhancement in light harvest and photocurrent generation of the devices over a broad wavelength range. In addition, the 1D GNP structure increases the *FF* by improving electron extraction and suppressing charge recombination due to increased interfacial contact area between mp-TiO_2 and $CsPbIBr_2$, where excitons are separated and charge transfer occurs. As a result, the PSCs with 1D GNP mp-TiO_2 gained a *PCE* of 4.31%, which is almost 23% higher than that of the flat mp-TiO_2 PSCs (3.5%).

We believe that nanoimprinting a 1D GNP structure on the mp-TiO_2 photoelectrode, which optimizes the light harvest, can be an effective way to improve the photoelectric properties in various types of perovskite-based optoelectronic devices, such as solar cells, photodetectors, light-emitting diodes, and solar water-splitting devices.

Abbreviations

CsPe: Cesium based all inorganic halide perovskite; HPe: Organic-inorganic hybrid halide perovskite; 1D GNP: One-dimensional grating nanopattern; PSC: Perovskite solar cell; FTO: Fluorine-doped tin oxide; bl-TiO_2: Blocking TiO_2; mp-TiO_2: Mesoporous TiO_2; PDMS: Polydimethylsiloxane; HTLs: Hole transport layers; J_{SC}: Short-circuit current density; V_{OC}: Open-circuit voltage; *FF*: Fill factor; *PCE*: Power conversion efficiency; *J*– *V*: Current density–voltage; FE-SEM: Field-emission scanning electron microscopy; XRD: X-ray diffraction; EQE: External quantum efficiency; UV-Vis: Ultraviolet–visible spectrometer; R_S: Series resistance; R_{SH}: Shunt resistance; PTB7: Poly[[4,8-bis[(2-ethylhexyl)oxy]benzo[1,2-b:4,5-b']dithiophene-2,6-diyl][3-fluoro-2-[(2-ethylhexyl)carbonyl]thieno[3,4-b]thiophenediyl]]; PFOCTS: Trichloro(1H,1H,2H,2H-perfluorooctyl)silane.

Declarations

Availability of data and materials

The datasets used and/or analysed during the current study are available from the corresponding author on reasonable request.

Competing Interests

The authors declare that they have no competing interests.

Funding

This study was supported by the DGIST R&D Program of the Ministry of Science and ICT of Korea (20-ET-08), and the National Research Foundation of Korea (NRF) grant funded by the Korea government (MSIT)

(NRF-2019R1C1C1007569).

Author's Contributions

KPK and SW executed idea conceptualization and experimental design. KPK, SMK, and WHK performed the experiments. SW prepared the manuscript. KPK, SMK, and SW performed the main data analysis. All authors read and approved the final manuscript.

Acknowledgements

We would like to thank Editage (www.editage.co.kr) for English language editing.

References

[1] Park NK. Research direction toward scalable, stable, and high efficiency perovskite solar cells. Adv Energy Mater. 2020;10:1903106.

[2] Best Research-Cell Efficiency Chart. National Renewable Energy Laboratory (NREL), 2020. https://www.nrel.gov/pv/cell-efficiency.html. Accessed 18 Sept 2020.

[3] Huang J, Yuan Y, Shao Y, Yan Y. Understanding the physical properties of hybrid perovskites for photovoltaic applications. Nat Rev Mater. 2017;2:17042.

[4] Wang R, Mujahid M, Duan Y, Wang ZK, Xue J, Yang Y. A Review of Perovskites Solar Cell Stability. Adv Funct Mater. 2019;29:1808843.

[5] Cheacharoen R, Rolston N, Harwood D, Bush KA, Dauskardt RH, McGehee MD. Design and understanding of encapsulated perovskite solar cells to withstand temperature cycling. Energy Environ Sci. 2018;11:144-150.

[6] Chen J, Park NG. Materials and methods for interface engineering toward stable and efficient perovskite solar cells. ACS Energy Lett. 2020;5:2742-2786.

[7] Chan SH, Wu MC, Lee KM, Chen WC, Lin TH, Su WF. Enhancing perovskite solar cell performance and stability by doping barium in methylammonium lead halide. J Mater Chem A. 2017;5:18044-18052.

[8] Duan J, Xu H, Sha WEI, Zhao Y, Wang Y, Yang X, Tang Q. Inorganic perovskite solar cells: an emerging member of the photovoltaic community. J Mater Chem A. 2019;7:21036-21068.

[9] Ouedraogo NAN, Chen Y, Xiao YY, Meng Q, Han CB, Yan H, Zhang Y. Stability of all inorganic perovskite solar cells. Nano Energy. 2020;67:104249.

[10] Xiang W, Tress W. Review on recent progress of all-inorganic metal halide perovskites and solar cells. Adv Mater. 2019;31:1902851.

[11] Duan J, Hu T, Zhao Y, He B, Tang Q. Carbon-electrode-tailored all-Inorganic perovskite solar cells to harvest solar and water-vapor energy. Angew Chem Int Ed. 2018;57:5746-5749.

[12] Liang J, Zhao P, Wang C, Wang Y, Hu Y, Zhu G, Ma L, Liu J, Jin Z. $CsPb_{0.9}Sn_{0.1}IBr_2$ based all-inorganic perovskite solar cells with exceptional efficiency and stability. J Am Chem Soc. 2017;139:14009-14012.

[13] Wang Y, Zhang T, Kan M, Zhao Y. Bifunctional stabilization of all-inorganic alpha-$CsPbI_3$ perovskite for 17% efficiency photovoltaics. J Am Chem Soc. 2018;140:12345-12348.

[14] Straus DB, Guo S, Abeykoon AMM, Cava RJ. Understanding the instability of the halide perovskite $CsPbI_3$ through temperature-dependent structural analysis. Adv Mater. 2020;32:2001069.

[15] Liang J, Wang C, Wang Y, Xu Z, Lu Z, Ma Y, Zhu H, Hu Y, Xiao C, Yi X, Zhu G, Lv H, Ma L, Chen T, Tie Z, Jin Z, Liu J. All-inorganic perovskite solar cells. J Am Chem Soc. 2016;138:15829-15832.

[16] Mariotti S, Hutter OS, Phillips LJ, Yates PJ, Kundu B, Durose K. Stability and performance of $CsPbI_2Br$ thin films and solar cell devices. ACS Appl Mater Interfaces. 2018;10:3750-3760.

[17] Zeng Q, Zhang X, Liu C, Feng T, Chen Z, Zhang W, Zheng W, Zhang H, Yang B. Inorganic $CsPbI_2Br$ perovskite solar cells: The progress and perspective. Sol RRL. 2019;3:1800239.

[18] Guo Y, Yin X, Liu J, Wen S, Wu Y, Que W. Inorganic $CsPbIBr_2$-based perovskite solar cells: Fabrication technique modification and efficiency improvement. Sol RRL. 2019;3:1900135.

[19] Liu C, Li W, Chen J, Fan J, Mai Y, Schropp REI. Ultra-thin MoO_x as cathode buffer layer for the improvement of all-inorganic $CsPbIBr_2$ perovskite solar cells. Nano Energy. 2017;41:75.

[20] Zhu W, Zhang Q, Chen D, Zhang Z, Lin Z, Chang J, Zhang J, Zhang C, Hao Y. Intermolecular exchange boosts efficiency of air-stable, carbon-based all-inorganic planar $CsPbIBr_2$ perovskite solar cells to over 9%. Adv Energy Mater. 2018;8:1802080.

[21] Guo Y, Yin X, Liu J, Que W. Highly efficient $CsPbIBr_2$ perovskite solar cells with efficiency over 9.8% fabricated using a preheating-assisted spin-coating method. J Mater Chem A. 2019;7:19008-19016.

[22] Subhani WS, Wang K, Du M, Wang X, Liu S. Interface-modification-induced gradient energy band for highly efficient $CsPbIBr_2$ perovskite solar cells. Adv Energy Mater. 2019;9:1803785.

[23] Liang J, Liu Z, Qiu L, Hawash Z, Meng L, Wu Z, Jiang Y, Ono LK, Qi Y. Enhancing optical, electronic, crystalline, and morphological properties of cesium lead halide by Mn substitution for high-stability all-inorganic perovskite solar cells with carbon electrodes. Adv Energy Mater. 2018;1800504.

[24] Cui J, Chen C, Han J, Cao K, Zhang W, Shen Y, Wang M. Surface plasmon resonance effect in inverted perovskite solar cells. Adv Sci. 2016;3:1500312.

[25] Tavakoli MM, Tsui KH, Zhang Q, He J, Yao Y, Li D, Fan Z. Highly efficient flexible perovskite solar cells with antireflection and self-cleaning nanostructures. ACS Nano. 2015;9:10287.

[26] Luo Q, Deng X, Zhang C, Yu M, Zhou X, Wang Z, Chen Z, Huang S. Enhancing photovoltaic performance of perovskite solar cells with silica nanosphere antireflection coatings. Solar Energy. 2018;169:128.

[27] Wang Y, Wang P, Zhou X, Li C, Li H, Hu X, Li F, Liu X, Li M, Song Y. Diffraction-grated perovskite induced highly efficient solar cells through nanophotonic light trapping. Adv Energy Mater. 2018;1702960.

[28] Subhani WS, Wang K, Du M, Liu SF. Goldschmidt-rule-deviated perovskite $CsPbIBr_2$ by barium substitution for efficient solar cells. Nano Energy. 2019;61:165-172.

[29] Yang S, Wang L, Gao L, Cao J, Han Q, Yu F, Kamata Y, Zhang C, Fan M, Wei G, Ma T. Excellent moisture stability and efficiency of inverted all-inorganic $CsPbIBr_2$ perovskite solar cells through molecule interface engineering. ACS Appl Mater Interfaces. 2020;12:13931-13940.

[30] Liu Z, Li H, Qin C, Zhang T, Gu Y, Chen H, Zheng H, Li S. Solution-processed inorganic perovskite flexible photodetectors with high performance. Nanoscale Res Lett. 2019;14:284.

[31] Wooh S, Yoon H, Jung JH, Lee YG, Koh JH, Lee B, Kang YS, Char K. Efficient light harvesting with micropatterned 3D pyramidal photoanodes in dye-sensitized solar cells. Adv Mater. 2013;25:3111-3116.

[32] Kim J, Koh JK, Kim B, Kim JH, Kim E. Nanopatterning of mesoporous inorganic oxide films for efficient light harvesting of dye-sensitized solar cells. Angew Chem Int Ed. 2012;51:6864-6869.

[33] Mahpeykar SM, Xiong Q, Wang X. Resonance-induced absorption enhancement in colloidal quantum dot solar cells using nanostructured electrodes. Opt Express. 2014;22:A1576.

[34] Choi DH, Nam SK, Jung K, Moon JH. 2D photonic crystal nanodisk array as electron transport layer for highly efficient perovskite solar cells. Nano Energy. 2019;56:365-372.

[35] Jiang Y, Almansouri I, Huang S, Young T, Li Y, Peng Y, Hou Q, Spiccia L, Bach U, Cheng YB, Green MA, Ho-Baillie A. Optical analysis of perovskite/silicon tandem solar cells. J Mater Chem C. 2016;4:5679-5689.

[36] Jang S, Yoon J, Ha K, Kim MC, Kim DH, Kim SM, Kang SM, Park SJ, Jung HS, Choi M. Facile fabrication of three-dimensional TiO_2 structures for highly efficient perovskite solar cells. Nano Energy. 2016;22:499-506.

Figures

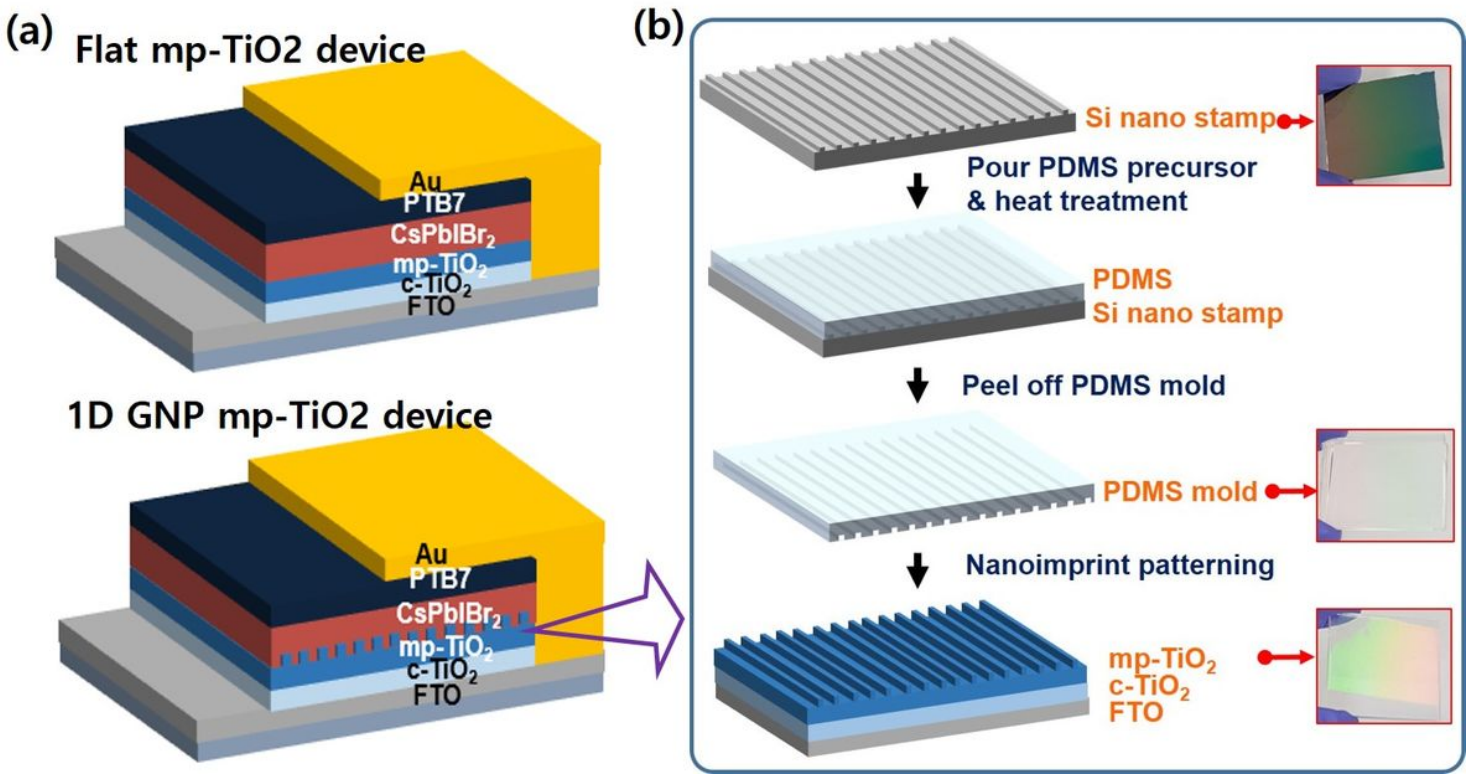

Figure 1

Schematics of (a) the device structure of CsPbIBr2 perovskite solar cells with a flat mp-TiO2 and a 1D GNP mp-TiO2, and (b) the fabrication process for 1D GNP mp-TiO2.

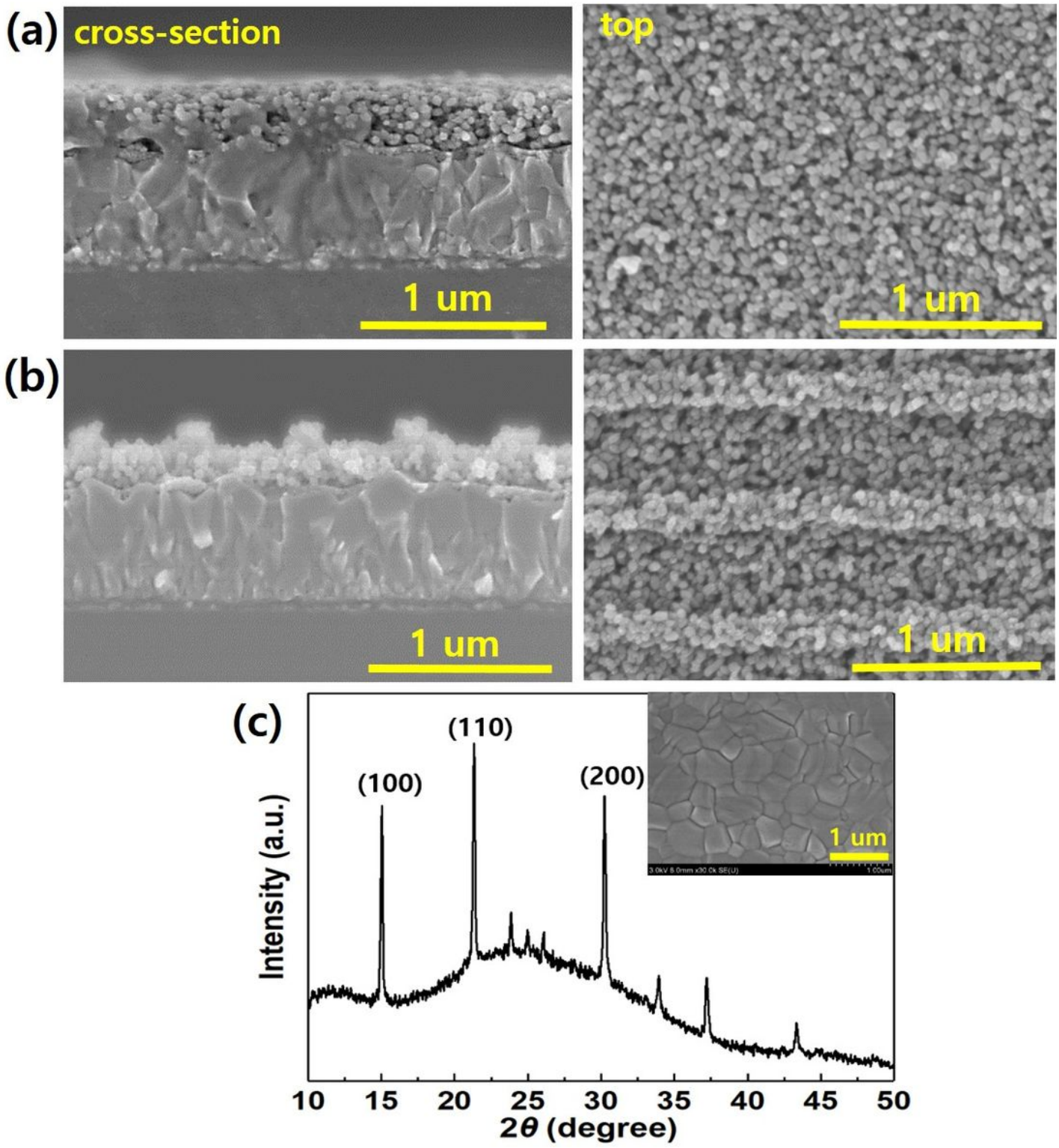

Figure 2

(a) Cross-section and top view SEM images of the flat mp-TiO2 and (b) 1D GNP mp-TiO2. (c) XRD data for CsPbIBr2 layer (inset is the surface morphology of the CsPbIBr2 layer).

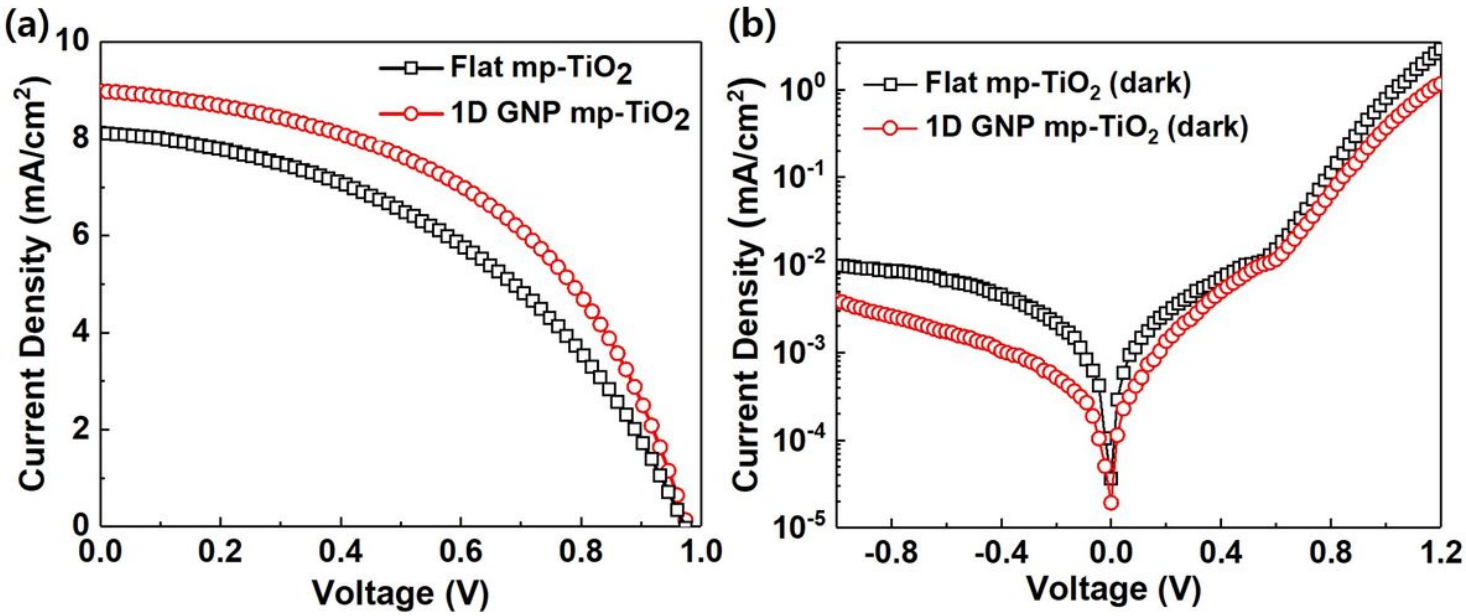

Figure 3

Current density–voltage (J–V) characteristics of CsPbIBr2 solar cells with a flat mp-TiO2 and a 1D GNP mp-TiO2 under (a) one sun illumination and (b) dark condition.

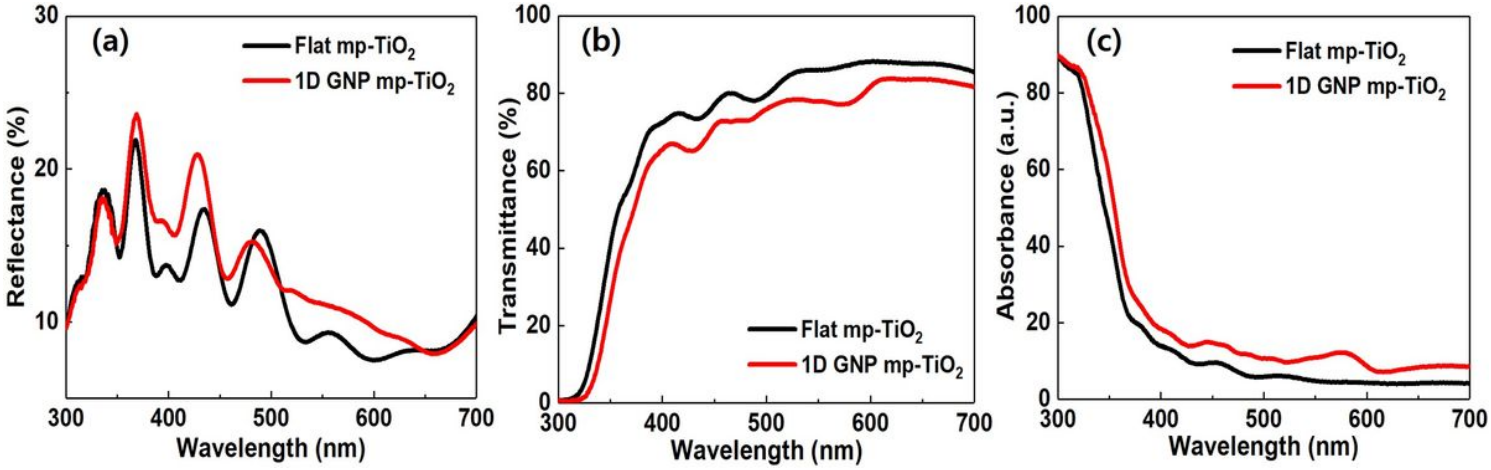

Figure 4

(a) Reflectance, (b) transmittance, and (c) absorbance spectra of the flat mp-TiO2 and 1D GNP mp-TiO2 layers.

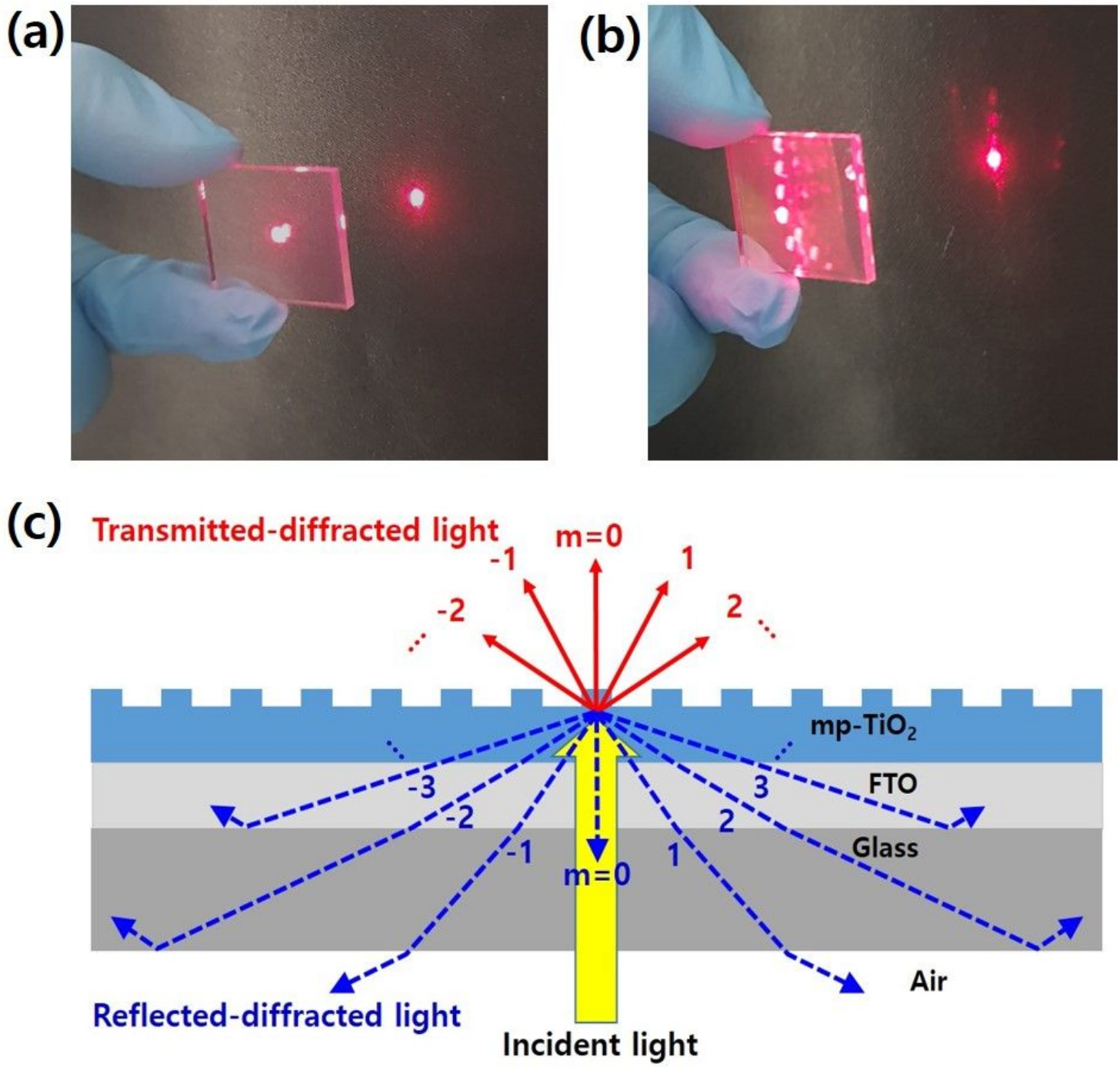

Figure 5

Digital camera images of diffracted light from (a) flat mp-TiO2 and (b) 1D GNP mp-TiO2, and (c) schematic illustration of grating diffraction.

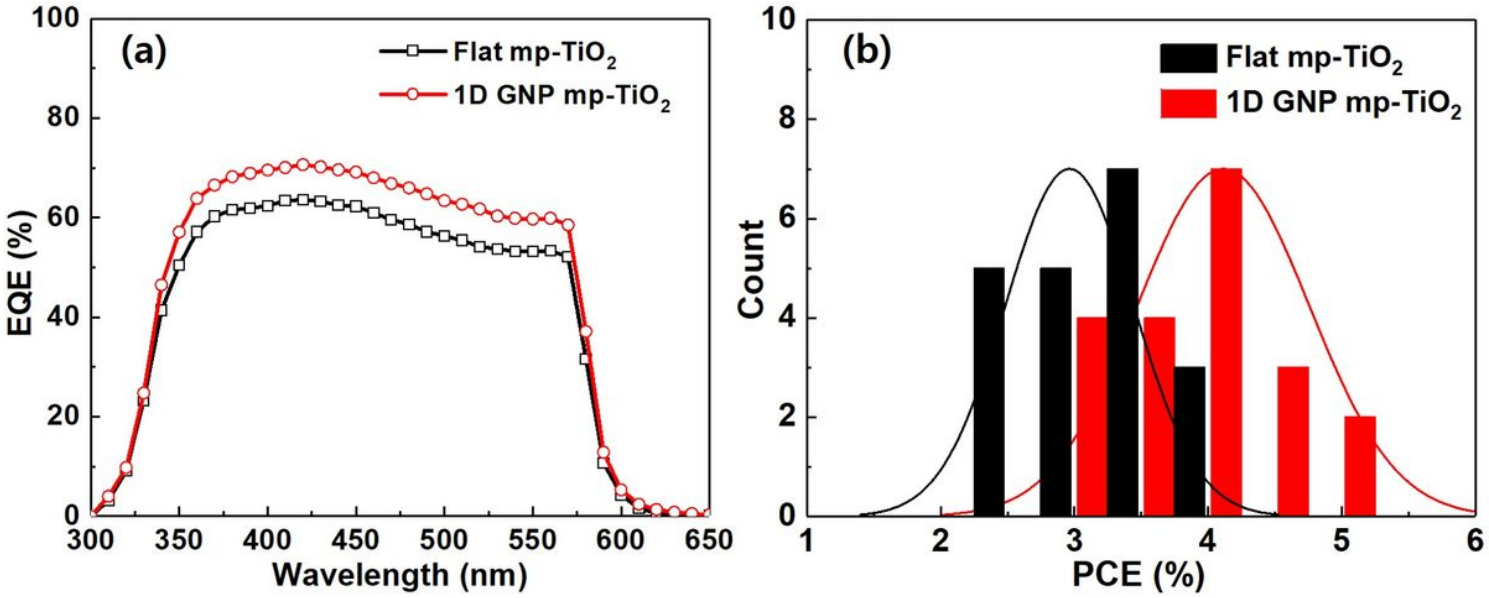

Figure 6

(a) External quantum efficiency (EQE) spectra and (b) PCE distribution histogram of the CsPbIBr2 PSCs with and without 1D GNP structure in mp-TiO2 for 20 devices.